


Tuning oxygen vacancies in $\text{Bi}_4\text{Ti}_3\text{O}_{12}$ nanosheets to boost piezo-photocatalytic activity

Journal Article

Author(s):

Tang, Qiao; Wu, Jiang; Chen, Xiang-Zhong; Sanchis-Gual, Roger; Veciana, Andrea; Franco, Carlos; Kim, Donghoon; Surin, Ivan; Pérez-Ramírez, Javier; Mattera, Michele; Terzopoulou, Anastasia; Qin, Ni; Vukomanović, Marija; [Nelson, Bradley](#) ; Puigmarti-Luis, Josep; Pané, Salvador

Publication date:

2023-04

Permanent link:

<https://doi.org/10.3929/ethz-b-000595231>

Rights / license:

[Creative Commons Attribution 4.0 International](#)

Originally published in:

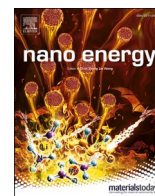
Nano Energy 108, <https://doi.org/10.1016/j.nanoen.2023.108202>

Funding acknowledgement:

192012 - Mechano-chromic, Voltage-sensitive Electrostimulators: Innovative Piezoelectric Biomaterials for Electro-stimulated Cellular growth (SNF)

181988 - Functional 2D porous crystalline materials (2DMats) (SNF)

771565C - Highly Integrated Nanoscale Robots for Targeted Delivery to the Central Nervous System (EC)



Tuning oxygen vacancies in Bi₄Ti₃O₁₂ nanosheets to boost piezo-photocatalytic activity

Qiao Tang^a, Jiang Wu^{a,b,*}, Xiang-Zhong Chen^a, Roger Sanchis-Gual^a, Andrea Veciana^a, Carlos Franco^a, Donghoon Kim^a, Ivan Surin^c, Javier Pérez-Ramírez^c, Michele Mattera^d, Anastasia Terzopoulou^a, Ni Qin^b, Marija Vukomanovic^e, Bradley J. Nelson^a, Josep Puigmartí-Luis^{f,g}, Salvador Pané^{a,**}

^a Multi-Scale Robotics Lab, Institute of Robotics and Intelligent Systems, ETH Zürich, Tannenstrasse 3, CH-8092 Zürich, Switzerland

^b State Key Laboratory of Optoelectronic Materials and Technologies, School of Materials Science and Engineering, Sun Yat-Sen University, 510275 Guangzhou, China

^c Institute for Chemical and Bioengineering, Department of Chemistry and Applied Biosciences, ETH Zürich, Vladimir-Prelog-Weg 1, 8093 Zürich, Switzerland

^d Department of Physical Chemistry, University of Barcelona, Martí i Franquès, 1, 08028 Barcelona, Spain

^e Advanced Materials Department, Jožef Stefan Institute, Jamova 39, 1000 Ljubljana, Slovenia

^f Departament de Ciència dels Materials i Química Física, Institut de Química Teòrica i Computacional, University of Barcelona (UB), 08028 Barcelona, Spain

^g Institució Catalana de Recerca i Estudis Avançats (ICREA), Pg. Lluís Companys 23, 08010 Barcelona, Spain

ARTICLE INFO

Keywords:

Oxygen vacancies
Piezo-photocatalysis
Bi₄Ti₃O₁₂
DFT
Dye degradation

ABSTRACT

Piezo-photocatalysis has emerged as a promising strategy to address environmental pollution and the fast-growing energy shortage. Unfortunately, current efficiencies of piezo-photocatalysts are still far from ideal, and improving their catalytic efficiency remains challenging. In this paper, we introduce oxygen vacancies (OVs) in Bi₄Ti₃O₁₂ (BIT) nanosheets to boost their piezo-photocatalytic performance. Compared to pristine BIT nanosheets, BIT with an optimized OV concentration exhibit excellent piezo-photocatalytic activity, with an enhancement of 2.2 times the degradation rate constant ($k = 0.214 \text{ min}^{-1}$) for Rhodamine B (RhB). The effect of OVs on the adsorption energy and Bader charges was also investigated using density functional theory (DFT) calculations, which shed light on the underlying mechanism that improves the piezo-photocatalytic process in the presence of OVs. Specifically, the introduction of OVs increases the adsorption energy and Bader charges, resulting in an enhancement of charge transfer between O₂/H₂O and BIT, thus facilitating the catalytic process. This study provides a deeper understanding into the regulation mechanism of OV enhanced piezo-photocatalytic activity and opens new avenues for designing high-performance piezo-photocatalysts.

1. Introduction

Over the last decades, long-standing industrialization processes have resulted in global energy misuse and severe environmental crises, thus posing a threatening challenge to the sustainable development of human society. To tackle this challenge, considerable attention has been focused on developing catalytic technologies that can utilize renewable and clean energy [1–6]. Among these catalytic technologies, photocatalysis has received extensive attention due to the pervasiveness and accessibility of light irradiation [7–13]. However, this promising catalytic technique still suffers from high recombination of photo-generated carriers [14,15], which significantly hampers the performance of

photocatalysts. Therefore, developing a technique to efficiently separate photo-generated carriers is critically important for improving the activity of photocatalysts. A relatively recent strategy consists of using catalysts that display both piezoelectricity and photocatalytic activity, a process known as piezo-photocatalysis, in which catalysts are simultaneously stimulated by mechanical vibrations and light irradiation. This approach allows for an efficient separation of the photo-generated carriers by means of piezoelectrically induced polarization. The piezoelectric field causes band bending at the solid-liquid electrolyte interface, which also favors the generation of free radicals. As a result, several piezoelectric semiconductors, such as BaTiO₃ [16], ZnO [17], BiFeO₃ [18], NaNbO₃ [19], and BiOCl [20], have been investigated for

* Corresponding authors at: Multi-Scale Robotics Lab, Institute of Robotics and Intelligent Systems, ETH Zürich, Tannenstrasse 3, CH-8092 Zürich, Switzerland

** Corresponding author.

E-mail addresses: jianwu@ethz.ch (J. Wu), vidalp@ethz.ch (S. Pané).

<https://doi.org/10.1016/j.nanoen.2023.108202>

Received 13 September 2022; Received in revised form 8 January 2023; Accepted 10 January 2023

Available online 11 January 2023

2211-2855/© 2023 The Authors. Published by Elsevier Ltd. This is an open access article under the CC BY license (<http://creativecommons.org/licenses/by/4.0/>).

their piezo-photocatalytic activity. Unfortunately, their catalytic efficiency is still far from ideal.

Several approaches have been proposed to enhance the activity of piezo-photocatalysts, such as by introducing heterojunctions [2], co-catalysts [21], or by changing the morphology of the catalysts [22]. These different approaches represent substantial progress in the research and development of piezo-photocatalysis. Defect engineering, particularly oxygen vacancy (OV) defect engineering, is an alternative route that has recently drawn considerable attention as it can alter energy band structure, enhance light absorption, and increase carrier concentration [23]. However, the influence of OVs on piezo-photocatalysis remains unclear, and understanding how OVs influence the piezo-photocatalytic performance is crucial for designing catalysts with improved piezo-photocatalytic activity.

$\text{Bi}_4\text{Ti}_3\text{O}_{12}$ (BIT) is one of the most appealing materials for applications in piezo-photocatalysis. BIT possesses a unique layered perovskite structure that is composed of $(\text{Bi}_2\text{O}_2)^{2+}$ and $(\text{Bi}_2\text{Ti}_3\text{O}_{10})^{2-}$ layers stacked alternately along the *c* axis, which allows growing BIT as a two-dimensional (2D) shape. This is a suitable architecture for maximizing deformation under mechanical vibrations [24]. Because of the hybridized valence band composed by Bi 6s and O 2p orbitals, BIT has a narrow bandgap, which facilitates the generation of electrons and holes [25]. Given its superior piezoelectric performance, layered crystal structure, and narrow band gap, BIT is considered a promising candidate for piezo-photocatalysis. In this work, we synthesized a series of BIT nanosheets with different OV concentrations and investigated their photocatalytic, piezocatalytic, and piezo-photocatalytic activities. With an optimum OV concentration, BIT showed a piezo-photocatalytic degradation rate of up to 0.214 min^{-1} , which is 2.2 times that of pristine BIT. Subsequently, the mechanism for enhanced catalytic activity was elucidated by density functional theory (DFT) calculations and active radical trapping experiments.

2. Experimental section

2.1. Preparation of catalysts

The $\text{Bi}_4\text{Ti}_3\text{O}_{12}$ nanosheets with adjustable OV concentrations were fabricated using a modified molten salt method [26]. NaCl and KCl were chosen as the cosolvents. Bi_2O_3 and TiO_2 were bismuth and titanium sources, while urea was used to create OVs [27]. The typical preparation procedure is described as follows: NaCl and KCl powders with the same mole ratio (62.5 mmol) were mixed and ground in a mortar for 10 min. Subsequently, Bi_2O_3 (5 mmol), TiO_2 (7.5 mmol), and an appropriate amount of urea were added and ground for another 1.5 h. The mixture was then transferred into an alumina crucible and calcined at 700°C for 2 h in air. The final product was washed repeatedly with distilled water, ethanol, and dried at 70°C overnight. According to the amount of urea added (0, 0.6, 1.2, and 1.8 g), the prepared BIT samples were labeled as BIT, BIT-OV1, BIT-OV2, and BIT-OV3.

2.2. Material characterization

The crystalline structures of the prepared samples were collected by X-ray diffraction (XRD, Bruker AXS D8 Advance, Cu Ka). The surface morphology was characterized using a scanning electron microscope (SEM, JSM-7100 F, JEOL). TEM images and elemental distribution data were obtained from transmission electron microscopy (TEM, Talos F200X, FEI) at an accelerating voltage of 150 kV. X-ray photoelectron spectra (XPS) were recorded on a Phoibos 150 analyzer (SPECS EAS10P GmbH) to confirm the chemical state. Electron paramagnetic resonance (EPR, JEOL JES-FA200) spectra were performed to detect the oxygen vacancies. Piezoresponse force microscopic (PFM) measurements were carried out by a commercial atomic force microscope (Ntegra Prima, NT-MDT). Temperature-programmed desorption of oxygen (O_2 -TPD) was performed on an AutoChem II 2920 (Micromeritics, USA) using a TCD

detector. The sample (0.1 g) was loaded into a U-shaped quartz micro-reactor, dried in He at 473 K (heating rate = 20 K/min, holding time = 60 min, total volumetric flow (F_T) = $20 \text{ cm}^3/\text{min}$) and cooled to 313 K. Subsequently, O_2 adsorption was carried out by flowing O_2 at 313 K (hold time = 60 min, F_T = $50 \text{ cm}^3/\text{min}$), followed by heating of the sample to 873 K (heating rate = 10 K/min) in flowing He (F_T = $20 \text{ cm}^3/\text{min}$). The piezo-photoelectrochemical tests were carried out on an electrochemical workstation (PGSTAT204, Metrohm, Zofingen, Switzerland) using a standard three-electrode system with a working electrode, a carbon rod as the counter electrode, and Ag/AgCl as the reference electrode, respectively. 2.5 mg of sample was dispersed into 30 μL of ethanol and 70 μL of Nafion. The mixture was completely drop-coated on the surface of indium tin oxide (ITO) glass and dried in the air for 24 h. The measured sample-coated electrode area is 1 cm^2 and Na_2SO_4 (0.5 M) was selected as the electrolyte.

2.3. Degradation of dye pollutants

The degradation of rhodamine B (RhB) dye molecules was used to assess the piezo-photocatalytic activity of the BIT catalysts. Typically, 80 mg of the catalysts were dispersed into 80 mL of RhB aqueous solution (5 mg/L). Prior to reaction, the suspension was subjected to an ultrasonic bath to make the catalyst disperse well, and then stirred for 30 min in the dark to reach an adsorption-desorption equilibrium between the catalysts and RhB molecules. The suspension was subjected to visible light (Asahi Spectra, MAX-303, 300 W, $300 \text{ nm} < \lambda < 600 \text{ nm}$) and ultrasonic vibration (Prima, PM1-300TD, 120 W, 40 kHz) simultaneously. The catalytic reaction system was kept at $25 \pm 1^\circ\text{C}$. At a specific time interval, 1 mL of residual suspension was centrifuged for UV-vis absorption analysis through a UV-Vis spectrophotometer (Tecan Infinite 200 Pro).

2.4. Detection of free radicals

To explore the role of active species in the catalytic process, radical scavengers, including tert-butyl alcohol (0.2 M, TBA), benzoquinone (0.15 M, BQ), and disodium ethylenediaminetetraacetate (0.2 M, EDTA-2Na), were added into the catalytic system to capture hydroxyl radicals ($\bullet\text{OH}$), superoxide radicals ($\bullet\text{O}_2^-$) and holes (h^+), respectively. The concentration of $\bullet\text{OH}$, $\bullet\text{O}_2^-$, and H_2O_2 in an aqueous solution was further quantified by terephthalic acid photoluminescence (TA-PL) [3,28], nitroblue tetrazolium (NBT) transmission [29,30], and iodide method, respectively [31].

2.5. DFT calculations

In this work, all density functional theory (DFT) with spin polarization calculations were implemented in the Vienna Ab Initio Simulation Package (VASP) code. The Perdew-Burke-Ernzerhof (PBE) functional within the generalized gradient approximation (GGA) was adopted to describe electronic exchange-correlation energy. The ionic cores were described with the projector augmented wave (PAW) method. The calculated 2×2 supercell structures were the periodic boundary conditions in the *x*- and *y*-directions. And in the *z*-direction, the structure was separated by 15 Å vacuum height from its neighbors. A basis set of plane waves was determined by an energy cutoff of 450 eV. For the structure optimization and energy calculations, the K-points were set at $2 \times 2 \times 1$. All of the calculations were continued until the force and energy converged at less than 0.02 eV \AA^{-1} and 10^{-5} eV , respectively. The O_2 and H_2O adsorption processes were also investigated with DFT calculations to obtain the adsorption energy (ΔE_{ads}), and using the following formula:

$$\Delta E_{\text{ads}} = E_{\text{base-ads}} - (E_{\text{base}} + E_{\text{ads}})$$

where $E_{\text{base-ads}}$, E_{base} , and E_{ads} represent the total energy of

base-adsorption species, base, and adsorption species, respectively.

3. Results and discussion

3.1. Synthesis and characterization

The crystalline structure of the prepared BIT samples was investigated and confirmed by XRD analysis. As shown in Fig. 1a, all the diffraction peaks can be well-indexed to the orthorhombic phase of $\text{Bi}_4\text{Ti}_3\text{O}_{12}$ (JCPDS 72-1019), indicating the high crystallinity and purity of the prepared samples without the existence of other phases such as TiO_2 and Bi_2O_3 . Unlike the standard pattern where (117) shows the highest peak intensity, the main diffraction peaks in our BIT samples are (00 n) ($n = 4, 6, 8, 12, 14$ et al.), implying that the main exposed surface of the BIT samples is {00 n } [32]. This is mainly because the layered crystal structure of BIT creates low bonding energy between layers along the c -axis, driving the growth units to spread outwards along a plane perpendicular to the c -axis, thus showing the large exposure of {00 n } facets. To further verify the samples' morphology and obtain insightful information from the microstructures, SEM and TEM images were acquired. As shown in Figs. 1b-f and S1, all the prepared BIT samples display similar square nanosheet shapes with a length of 2–4 μm and a width of 1.5–2.5 μm . The high-resolution TEM (HRTEM) image of BIT-OV1 in Fig. 1g displays two sets of lattice fringes with an average spacing of 0.275 and 0.278 nm, which index well with the interplanar distance of (020) and (002) crystal plane of orthorhombic $\text{Bi}_4\text{Ti}_3\text{O}_{12}$. The corresponding selected area electron diffraction (SAED) pattern (Fig. 1h) further confirms the single crystalline nature of BIT-OV1. To have a clear understanding of the elemental distribution, the energy-dispersive spectroscopy (EDS) elemental mapping was carried out. As seen in Fig. 1i, Bi, Ti, and O elements were detected and dispersed throughout the whole nanosheet. The corresponding EDS

profile demonstrates that no other elements or impurities were observed, with the exception of the Cu from the sample holder.

XPS analysis was carried out to investigate the surface chemical states and OVs in the as-prepared BIT samples. The signals of Bi, Ti, O and C were observed in the survey spectra (Fig. 2a), confirming the chemical composition of $\text{Bi}_4\text{Ti}_3\text{O}_{12}$. The additional C element may originate from the adventitious carbon in the air or instrument. As shown in Fig. 2d-g, the O 1s peak can be deconvoluted into two peaks at 529.4 and 531.2 eV, corresponding to lattice oxygen and OVs, respectively [20,33]. As expected, with the increased usage of urea, the proportion of OVs peak gradually increased from 5.2% to 9.8%. In contrast to previously reported XPS spectra of Bi^{3+} [34], two new peaks that belong to Bi suboxide (an oxidation state of (+3- x) state) were observed near 158.1 and 163.5 eV (Fig. 2b), which are typically attributed to the existence of OVs in the vicinity of bismuth cations [33,35]. As for the Ti 2p spectra (Fig. 2c), the sharp peak at 457.8 eV can be assigned to Ti 2p_{3/2}, while the broad peak can be split into two peaks at 462.6 and 465.6 eV, referring to Ti 2p_{1/2} and Bi 4d_{3/2}, respectively [20]. To provide direct evidence for the existence of OVs, EPR analysis was also carried out. As displayed in Fig. 2h, the BIT samples possess obvious EPR signals centered at $g = 2.001$, which is typically identified as the characteristic signal of electrons trapped in OVs [36,37]. Based on the EPR signal intensity, the concentration of OVs in BIT samples can be determined in the following order: BIT-OV3 > BIT-OV2 > BIT-OV1 > BIT, which is consistent with the tendency shown in XPS patterns. These results indicate that OVs were successfully generated into the BIT, and their concentration gradually increased with the addition of urea.

Theoretically, due to the asymmetric crystal structure of BIT, piezoelectric potential can be detected on the surface of BIT when external pressure or stress is applied. To understand how the piezoelectric potential drives the piezo-photocatalysis, the piezoelectric response of the BIT and BIT-OV1 nanosheet was investigated by PFM

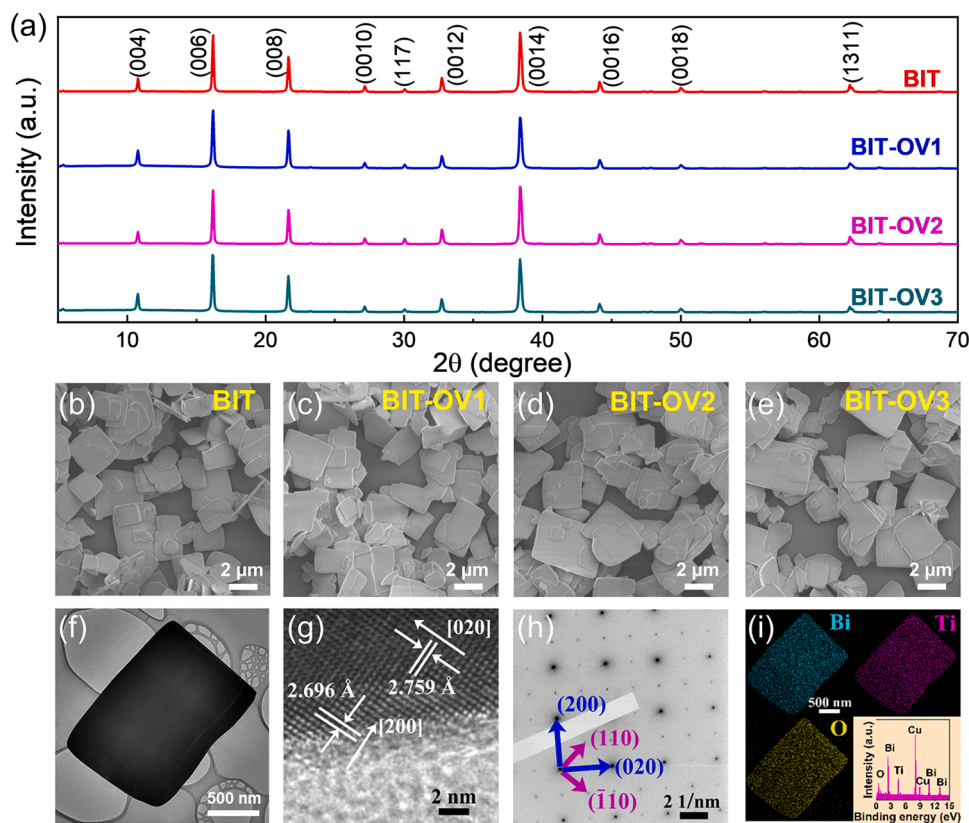


Fig. 1. Characterization of the prepared BIT samples: (a) XRD patterns, (b-e) SEM images of BIT, BIT-OV1, BIT-OV2, and BIT-OV3. (f) TEM image, (g) HRTEM image, (h) SAED pattern, and (i) EDX mapping images of BIT-OV1.

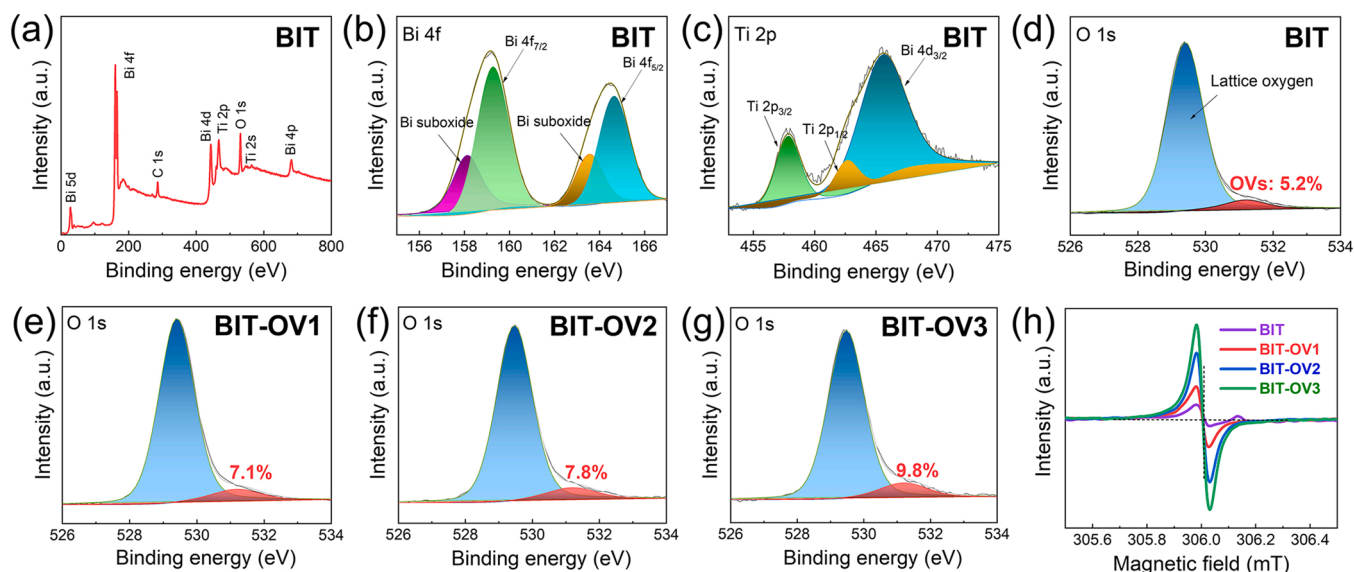


Fig. 2. (a) The full survey spectra, (b) XPS high-resolution Bi 4f, (c) Ti 2p, (d-g) O 1s, (h) EPR spectra.

contact mode. From the morphology image in Fig. 3a, a regular rectangular shape of BIT-OV1 was observed, which is consistent with the SEM and TEM images. The corresponding piezo-response amplitude (Fig. 3b) and phase images (Fig. 3c) exhibit distinct contrast variations, suggesting that BIT-OV1 possesses superior piezoelectric response. Moreover, a typical amplitude-voltage butterfly curve (Fig. 3d) and a well-defined hysteresis of 180° phase change were identified by applying a ± 10 V ramp voltage loop. The PFM results provide reliable proof that BIT-OV1 exhibits piezoelectricity.

The optical properties of BIT-based nanosheets were investigated by diffuse reflectance UV-vis spectra (DRS) spectra. As shown in Fig. S2, all the BIT samples have the same photo-absorption edges around 450–500 nm. According to the Kubelka-Munk model, the optical

bandgaps of BIT, BIT-OV1, BIT-OV2, and BIT-OV3 are determined to be 3.16, 3.19, 3.16, and 3.18 eV, respectively.

3.2. Catalytic activity performance

Encouraged by the adjustable OVs concentration in BIT, the effect of OVs on piezocatalytic, photocatalytic, and piezo-photocatalytic performance for RhB degradation was carried out. As shown in Fig. 4, with the application of light or ultrasonic vibration, almost no change in C/C_0 value was observed, suggesting that photolysis and sonolysis make little contribution to the degradation of RhB. In contrast, when BIT samples working together with external excitation (light or ultrasonic vibration), obvious degradation was detected, in which RhB was completely

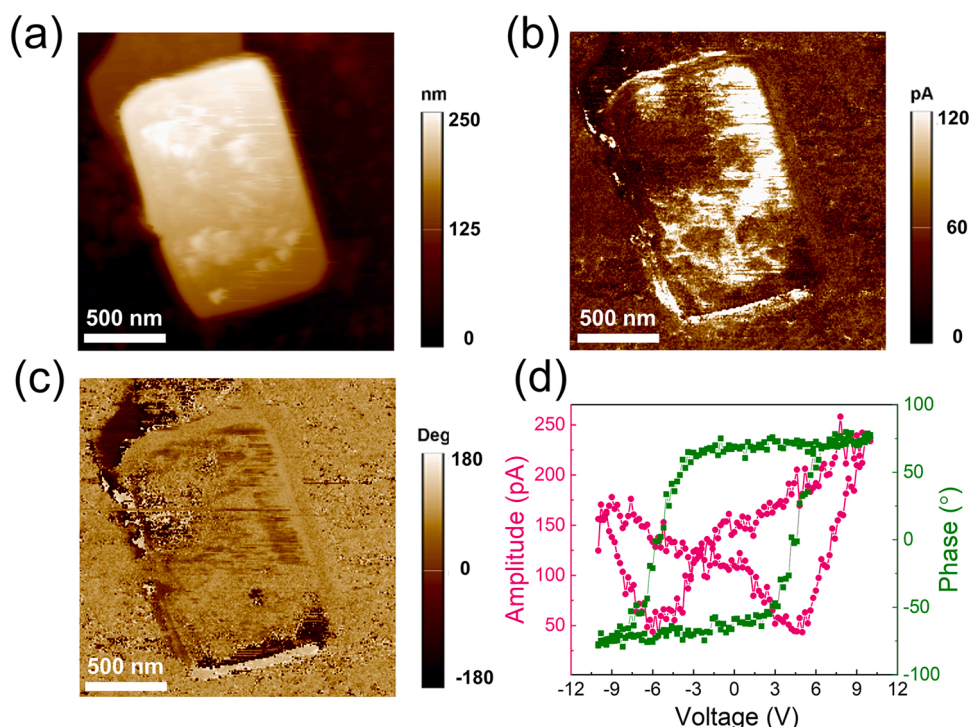


Fig. 3. Piezoelectric properties of BIT-OV1: (a) Morphology image. (b) Amplitude image. (c) Phase image. (d) Amplitude butterfly loop and phase hysteresis loop.

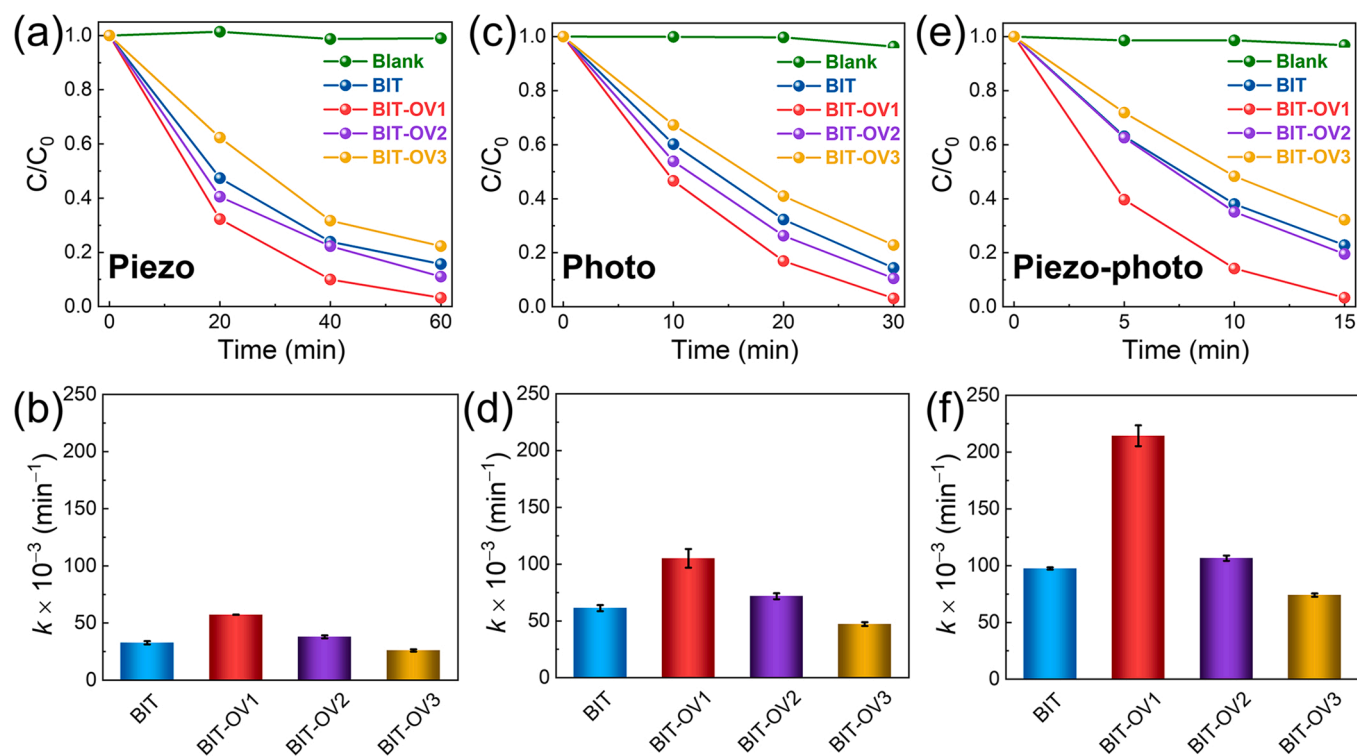


Fig. 4. (a–b) The piezocatalytic activities, (c–d) photocatalytic activities, and (e–f) piezo-photocatalytic activity of BIT, BIT-OV1, BIT-OV2, and BIT-OV3 for RhB degradation.

degraded over BIT-OV1 in 60 min, 30 min, and 15 min through piezocatalysis, photocatalysis, and piezo-photocatalysis with rate constants k of 0.057 min^{-1} , 0.105 min^{-1} , and 0.214 min^{-1} , respectively. The rate constant k of piezo-photocatalysis is significantly enhanced compared to the sum of piezocatalysis and photocatalysis, indicating the strong coupling effect between piezoelectric effect and photocatalysis. In addition to this, OVs also show a significant enhancing effect on the catalytic performance. As illustrated in Fig. 4b, d, and f, the catalytic activities of BIT display a maximum with increasing concentration of OVs. Compared to other BIT samples, the BIT-OV1 possesses an optimal k value, which is about 2 times higher than that of pristine BIT, implying the significant role of OVs in promoting catalytic performance. It is also important to note that, as the OVs concentration increased, the catalytic activity of BIT-OV2 and BIT-OV3 gradually decreased rather than increased. The above results indicate that only appropriate OVs concentration was aided to boost the catalytic performance, whereas high OVs concentration may instead weaken catalytic performance. A similar effect of OVs on piezocatalytic performance, also known as “volcano-type”, was reported in BaTiO_3 [38]. This may originate from the dual effect of OVs on catalytic performance. That is, OVs can have some positive effects on catalytic performance, such as increasing adsorption energy and decreasing reaction energy; however, they may also bring some negative effects that weaken the catalytic performance, such as decreasing piezoelectric performance and forming electron-hole complex centers. A more detailed discussion will be carried out later in the DFT theoretical calculation section. In addition, the piezo-photocatalytic stability of BIT-OV1 was also investigated in cycling runs, and the results were shown in Fig. S3. No obvious decrease in degradation efficiency was observed after recycling three times. The change in morphology and crystalline structure of BIT-OV1 before and after the piezo-photocatalytic reaction were characterized by SEM (Fig. S4), XRD (Fig. S5), and XPS (Fig. S6), respectively. These results indicate no noticeable change after cycling piezo-photocatalysis, suggesting the BIT-OV1 is stable. To investigate the effect of pH values on the piezo-photocatalytic degradation of RhB over BIT-OV1, NaOH or

HCl was added in the catalytic system to adjust the pH values. As depicted in Fig. S7, the degradation of RhB shows an increasing trend in acidic environments ($\text{pH} < 6.5$) and a decreasing trend in alkaline environments ($\text{pH} > 6.5$). The difference in BIT’s degradation efficiency may be explained by the adsorption capacity of BIT on RhB under different pH values [39]. That is, in alkaline environments, the adsorption ability between RhB molecules and BIT decreases sharply, thus leading to a lower piezo-photocatalytic degradation efficiency. These results indicate that BIT-based samples are more suitable for piezo-photocatalysis in neutral or acidic environments.

Dye degradation during catalysis is caused by reactive oxygen species, such as hydroxyl radicals and superoxide radicals. [40,41]. Therefore, we investigated the role of radicals in the catalytic mechanism by performing trapping experiments using scavengers. Typically, scavengers, including TBA, BQ, and EDTA-2Na, were chosen to capture $\bullet\text{OH}$, $\bullet\text{O}_2^-$, and h^+ , respectively. As shown in Fig. 5a and b, the piezocatalytic degradation of RhB was vastly inhibited by adding the above-mentioned scavengers, indicating that both $\bullet\text{OH}$, $\bullet\text{O}_2^-$ and h^+ were the main active species. Similarly, the addition of BQ and EDTA-2Na also resulted in a significant suppression of the photocatalytic degradation, while a slight effect was obtained when TBA was added (Fig. 5c and d). As for piezo-photocatalysis (Fig. 5e and f), the effect of scavengers on the catalytic performance was similar to that of photocatalysis, with the exception of the enhanced inhibitory ability of TBA. These results confirm that both $\bullet\text{O}_2^-$ and h^+ have a major role in piezocatalysis, photocatalysis, and piezo-photocatalysis, with the difference being that $\bullet\text{OH}$ shows a significant suppression on piezocatalysis, weak on photocatalysis, and moderate on piezo-photocatalysis.

To elucidate the differences in the mechanism between piezocatalysis and photocatalysis, the reactive oxygen species (ROS) production, including $\bullet\text{O}_2^-$, $\bullet\text{OH}$, and H_2O_2 , was conducted and presented in Figs. 6, S8, and S9. First, NBT was employed to evaluate the concentration of $\bullet\text{O}_2^-$ over the prepared BIT samples. As shown in Fig. 6a and d, $\bullet\text{O}_2^-$ was continuously generated with the application of ultrasonic vibration and light irradiation, and the production rate also shows a maximum with

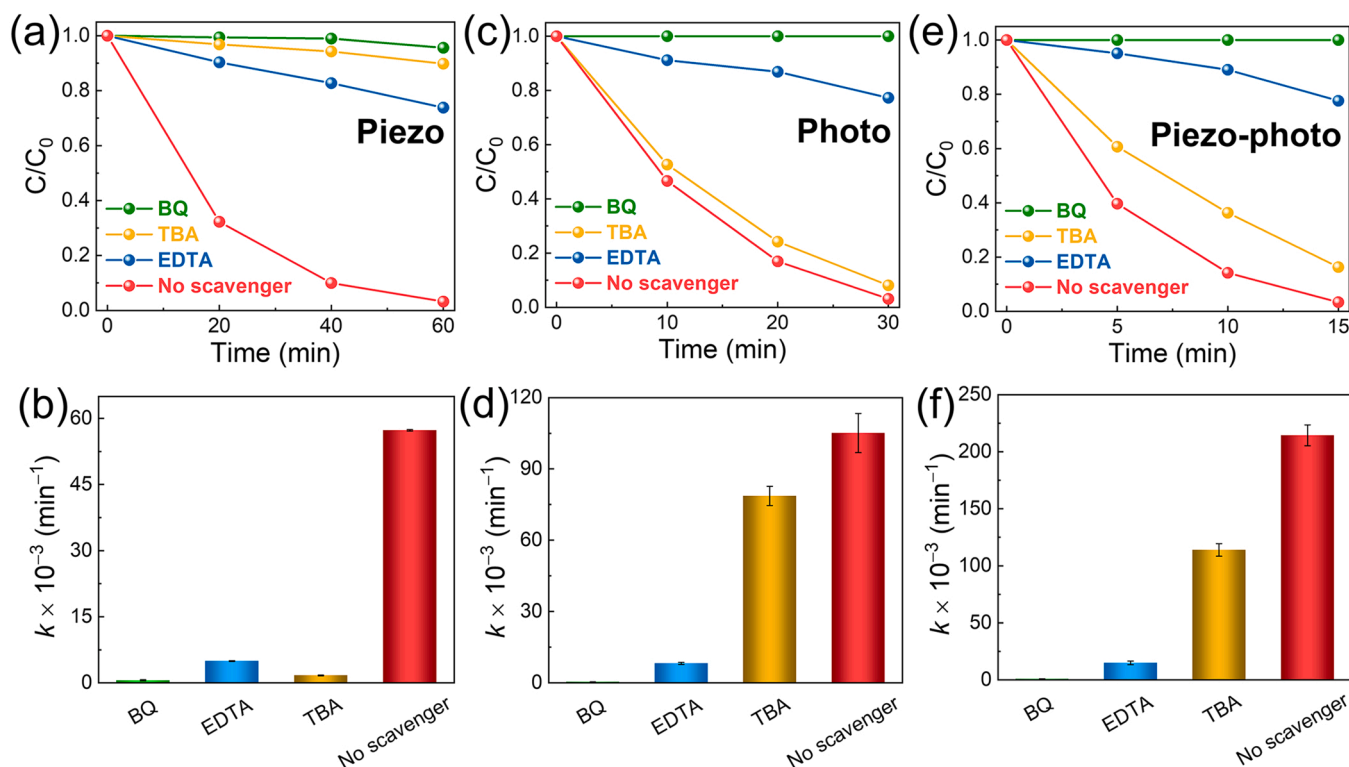


Fig. 5. Trapping experiments for the degradation of RhB over BIT-OV1: (a) Degradation dynamic curves under ultrasonic vibration and (b) corresponding rate constants k . (c) Degradation dynamic curves under light irradiation and (d) corresponding rate constants k . (e) Degradation dynamic curves under simultaneous light and ultrasonic vibration and (f) corresponding rate constants k .

increasing OVs, which agrees well with the RhB degradation results. Second, the concentration of $\bullet\text{OH}$ was monitored by the terephthalic acid photoluminescence (TA-PL) method (Fig. 6b and e). It is interesting to note that almost no $\bullet\text{OH}$ was detected in the photocatalytic process [42], while the yield of $\bullet\text{OH}$ increased rapidly in the piezocatalytic process. The generation of H_2O_2 was detected by the iodide method using ammonium molybdate (Fig. 6c and f). Similarly, a low production of H_2O_2 was obtained under light irradiation, whereas a high H_2O_2 production was observed under ultrasonic vibration. This phenomenon indicated that the light-induced photocatalysis over BIT cannot generate $\bullet\text{OH}$ and H_2O_2 , whereas piezocatalysis does. Theoretically, the valence band (VB) position of BIT is more negative than the potentials of $\bullet\text{OH}/\text{H}_2\text{O}$ (2.27 eV vs. NHE) [43], which prevents electron transfer between VB and H_2O (Fig. 6i). In the case of piezocatalysis, the electric field can tilt the energy band, and bring VB closer to $\bullet\text{OH}/\text{H}_2\text{O}$, thus allowing the electron transfer and the generation of $\bullet\text{OH}$. In addition, the production of $\bullet\text{O}_2^-$, $\bullet\text{OH}$, and H_2O_2 under piezo-photocatalysis was investigated. As shown in Fig. S10, the production rate of $\bullet\text{O}_2^-$, $\bullet\text{OH}$, and H_2O_2 show the highest for BIT-OV1, which is consistent with the trend in piezocatalysis and photocatalysis. Interestingly, under simultaneous light and ultrasound stimulation, the yield of $\bullet\text{O}_2^-$ shows a synergistic enhancement effect, while the yield of $\bullet\text{OH}$ and H_2O_2 were lower than that under individual ultrasonic irradiation. This phenomenon might be related to the fact that little $\bullet\text{OH}$ and H_2O_2 was generated by BIT when exposed to light irradiation. However, the specific mechanism need to be further explored in the future.

To further understand the charge transport characteristics, the transient current measurements of BIT-OV1 were performed under light with or without ultrasonic vibration applied. As shown in Fig. S11, the photocurrent was obviously enhanced with the application of ultrasound, indicating a higher separation efficiency of interfacial charge carriers. Both the generated photocurrent and piezo-photocurrent were reproducible as the external stimulations (light or light + ultrasonic

vibration) were switched on and off during three circulations. Moreover, the higher piezo-photocurrent value reveals that piezoelectric action promotes the efficiency of charge carriers' separation.

3.3. The mechanism for enhanced catalytic activity

To understand the influence of OVs on the piezo-photocatalytic activity of BIT, the charge difference distribution, absorption energy, and Bader charges were calculated by DFT. The BIT with different OVs concentration was constructed by removing one (BIT-OV1), two (BIT-OV2) or three oxygen atoms (BIT-OV3) from the BIT, respectively. The charge difference of O_2 and H_2O on ideal BIT and BIT-OV1 are illustrated in Figs. 7a-b and 7d-e, in which the blue and yellow regions represent electron accumulation and depletion. Compared with ideal BIT, the charge interaction between BIT-OV1 and $\text{O}_2/\text{H}_2\text{O}$ is much stronger, which can facilitate the following ROS generation reaction. Considering the important role of adsorption and electron transfer in the formation of free radicals, we also calculated the adsorption energy and Bader charges of O_2 and H_2O with different OVs concentrations. As shown in Fig. 7c and g, the adsorption energy (E_{ads}) of O_2 on BIT enhanced from 0.035 to -0.847 eV with increasing the OVs concentration, whereas the E_{ads} of H_2O increased from -1.325 to -1.504 eV. The increasing negative E_{ads} indicates that OVs can significantly enhance the thermodynamic priority for H_2O and O_2 adsorption. Additionally, the Bader charge analysis in Fig. 7d and h shows a positive proportional increase between Bader charge and OVs concentration, implying that OVs contribute to the charge transfer between the BIT and $\text{O}_2/\text{H}_2\text{O}$. Next, the O_2 temperature-programmed desorption (O_2 -TPD) was performed to complement DFT calculations. As illustrated in Fig. S12, the O_2 -TPD curves could be classified into two kinds of oxygen species following the temperature range of 250–450 and 450–600 °C, which could be assigned to surface active oxygen ions O_2^- and O^- , respectively [44]. Compared with the pristine BIT, it is clear that the BIT with more OVs

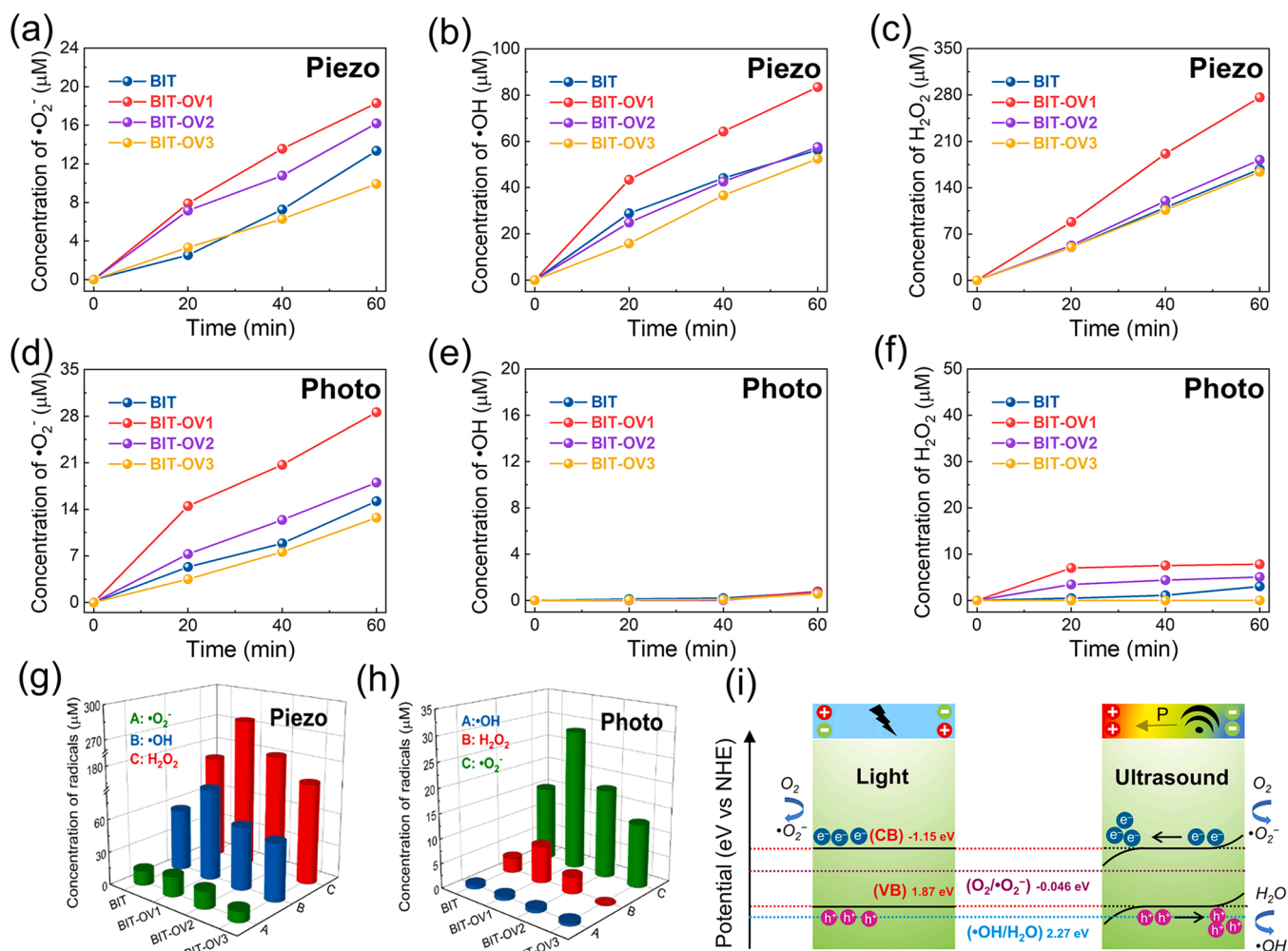


Fig. 6. (a–c) Under ultrasonic vibration, the concentration of $\bullet\text{O}_2^-$, $\bullet\text{OH}$, and H_2O_2 changes over time. (d–f) Under light irradiation, the concentration of $\bullet\text{O}_2^-$, (e) $\bullet\text{OH}$, and (f) H_2O_2 changes over time. (g) Comparisons of $\bullet\text{O}_2^-$, $\bullet\text{OH}$, and H_2O_2 concentrations after 60 min of ultrasonic vibration. (h) Comparisons of $\bullet\text{O}_2^-$, $\bullet\text{OH}$, and H_2O_2 concentrations after 60 min of light irradiation. (i) Diagram of the band structure of BIT and the mechanism of ROS generation under light irradiation or ultrasonic vibration.

exhibits stronger desorption peaks, indicating that BIT with more OVs can adsorb and activate more O_2 to form free radicals.

Based on these theoretical and experimental results, it is reasonable to expect that the introduction of OVs may result in a sustained enhancement in the catalytic activity. However, the reality is that while OVs can certainly enhance the catalytic performance but can also reduce it. The reason for the reduced catalytic activity may originate from the following factors: OVs may clamp the switching of electric dipoles, resulting in a low piezoelectric performance [38,45]; OVs may generate electron-hole recombination centers, limiting the separation of electron-hole pairs [46,47]. Consequently, OVs is a double-edged sword for catalytic activity, and introducing appropriate OVs is critical to optimizing the catalytic performance. To provide direct evidences for the decreased performance in piezo-responses of the pristine BIT and BIT-OV, the piezoelectric properties of both pristine BIT and BIT-OV were performed by PFM in the same parameters. As shown in Fig. S13 and Fig. S14, the amplitude and phase images of both BIT and BIT-OV1 display the clear contrast, indicating that both pristine BIT and BIT-OV1 are piezo-responsive. The representative amplitude-voltage butterfly curve and phase hysteresis loops were also recorded, verifying their piezoelectric nature. The intensity distribution of the amplitude signal is further provided to compare the piezoelectric properties between BIT and BIT-OV1. As shown in Fig. S15, the most probable distribution of piezoresponse amplitude for BIT is around 260 pA, which is much higher

than that of the BIT-OV1 (~ 195 pA).

Finally, a diagram showing the possible piezo-photocatalytic degradation mechanism of BIT-OV nanosheets is presented in Fig. 8. Under ultrasonic vibration, the BIT nanosheets were deformed by cavitation pressure and an electric field was built by accumulating positive and negative charges on opposite crystal surfaces. Under both light and ultrasonic vibration, the piezoelectric polarization and photo-generated carriers were generated simultaneously in BIT. Driven by piezoelectric polarization, the photo-generated carriers can effectively separate and rapidly migrate to the surface, which greatly lowers the recombination rate. Moreover, the piezoelectric polarization can also tilt the energy band, making the valence band more negative and the conduction band more positive. Therefore, when piezocatalysis and photocatalysis work together, a large number of electrons and holes can engage in the redox reaction with oxygen or water molecules, resulting in more free radicals and higher catalytic efficiency.

4. Conclusions

In this work, we have prepared $\text{Bi}_4\text{Ti}_3\text{O}_{12}$ nanosheets with tunable OVs concentration using a modified molten salt method and systematically investigated the influence of OVs on piezo-photocatalytic RhB dye degradation. With increasing OVs concentration, the piezo-photocatalytic activity exhibited a maximum for BIT-OV1 with the

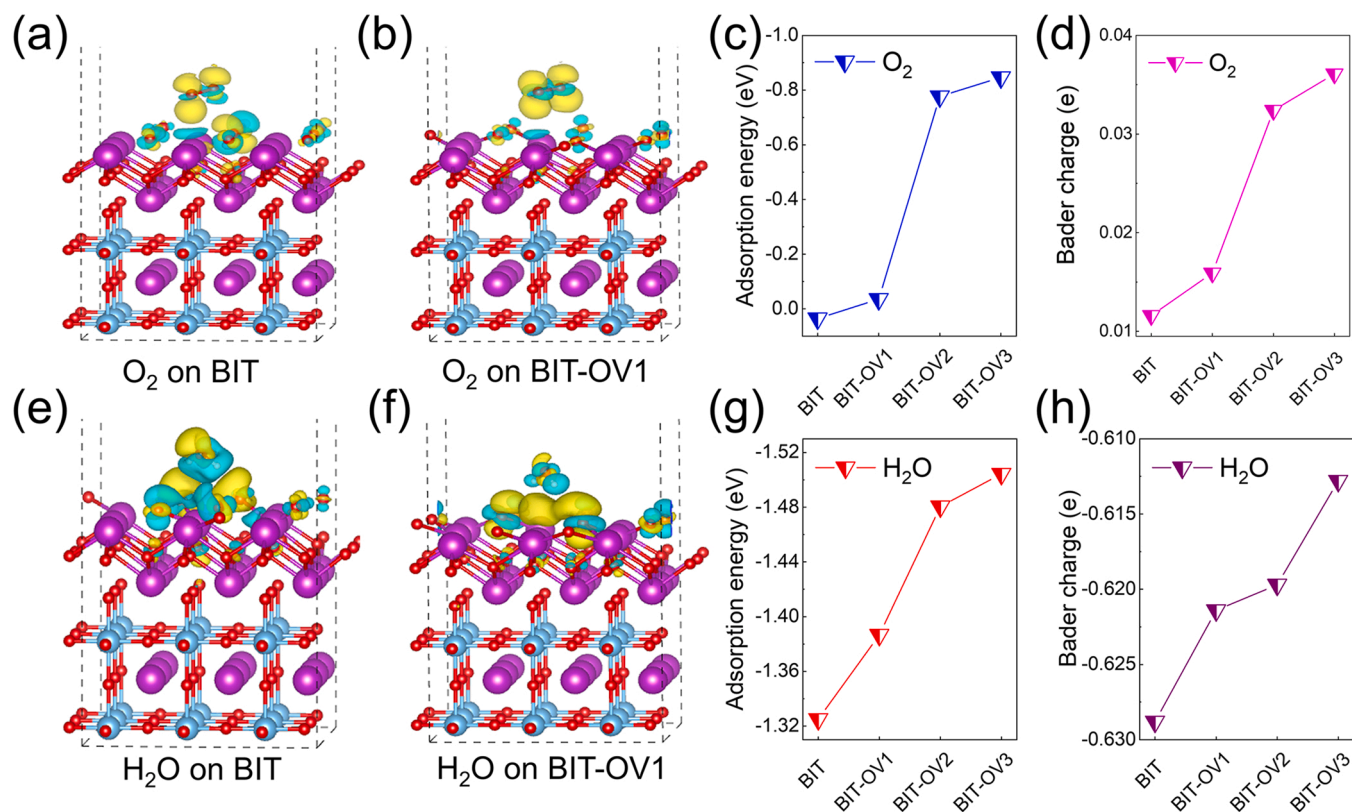


Fig. 7. Density functional theory calculations: Charge difference of O₂ adsorbed on (a) BIT and (b) BIT-OV1. (c) The adsorption energies and (d) Bader charge of O₂ on BIT, BIT-OV1, BIT-OV2, and BIT-OV3. Charge difference of H₂O adsorbed on (e) BIT and (f) BIT-OV1. (g) The adsorption energies and (h) Bader charge of H₂O on BIT, BIT-OV1, BIT-OV2, and BIT-OV3.

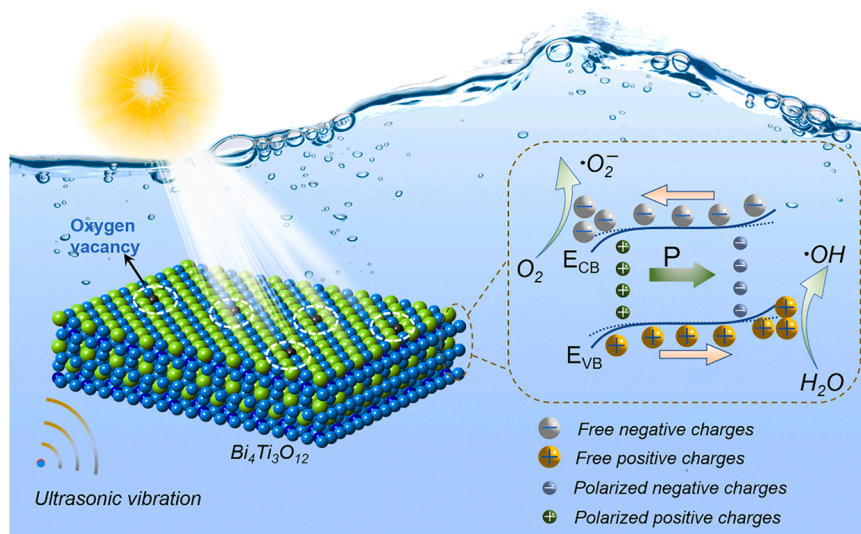


Fig. 8. Schematic illustration for the piezo-photocatalytic mechanism of BIT-OV.

highest k value (0.214 min^{-1}), which was about 2.2 times higher than that of pristine BIT (0.097 min^{-1}). The DFT calculations demonstrated that the introduction of OV can effectively enhance the adsorption energy and increase the Bader charges, facilitating the activation of ROS, such as •O₂⁻, •OH, and H₂O₂. By combining with light irradiation and ultrasonic vibrations, the BIT-OV1 exhibited an extraordinary piezo-photocatalytic degradation rate of 0.214 min^{-1} , which was about 2.1 and 4.1 times higher than that of photocatalysis and piezocatalysis, respectively. This work is expected to prompt a deeper understanding on

the influence of OVs on piezo-photocatalytic activity and may also provide a new approach for designing highly efficient catalysts that combine mechanical vibration and solar irradiation for pollutant degradation and ROS generation.

CRediT authorship contribution statement

Qiao Tang: Conceptualization, Methodology, Investigation, Writing – original draft, Writing – review & editing, Visualization. **Jiang Wu:**

Conceptualization, Methodology, Investigation, Writing – original draft, Writing – review & editing, Visualization, Supervision, Funding acquisition. **Xiang-Zhong Chen**: Conceptualization, Methodology, Investigation, Writing – original draft, Writing – review & editing, Supervision, Project administration, Funding acquisition. **Roger Sanchez-Gual**: Investigation, Writing – review & editing. **Andrea Veciana**: Investigation, Writing – review & editing. **Carlos Franco**: Investigation, Writing – original draft. **Donghoon Kim**: Investigation, Writing – original draft. **Ivan Surin**: Investigation, Resources, Writing – review & editing. **Javier Pérez-Ramírez**: Investigation, Writing – review & editing. **Michele Mattera**: Investigation, Writing – original draft. **Anastasia Terzopoulou**: Investigation, Writing – original draft. **Ni Qin**: Methodology, Investigation, Resources, Writing – review & editing. **Marija Vukomanovic**: Investigation, Resources, Writing – review & editing, Funding acquisition. **Bradley J. Nelson**: Investigation, Resources, Writing – review & editing, Supervision, Funding acquisition. **Josep Puigmartí-Luis**: Investigation, Writing – review & editing, Funding acquisition. **Salvador Pané**: Conceptualization, Investigation, Resources, Writing – review & editing, Supervision, Project administration, Funding acquisition.

Declaration of Competing Interest

The authors declare that they have no known competing financial interests or personal relationships that could have appeared to influence the work reported in this paper.

Data availability

Data will be made available on request.

Acknowledgments

This work has been financed by the ERC Consolidator Grant, European Union (No. 771565), the Swiss National Science Foundation, Switzerland (Project No. 192012), and the National Natural Science Foundation of China, China (No. 52102151). The authors would like to thank Lydia Zehnder from the Institute for Geochemistry and Petrology at ETH for her support on XRD measurements, the Scientific Center for Optical and Electron Microscopy (ScopeM), and FIRST laboratory at ETH for their technical support. M.V. acknowledges support from Slovenian Research Agency (ARRS) Grant, Slovenia (No. N-0150). J.P-L acknowledges support from the Swiss National Science Foundation (Project No. 200021_181988) and the grant PID2020–116612RB-C33 funded by MCIN/AEI /10.13039/501100011033. Q.T. acknowledges financial support from the China Scholarship Council, China (No. 201806780021).

Appendix A. Supporting information

Supplementary data associated with this article can be found in the online version at [doi:10.1016/j.nanoen.2023.108202](https://doi.org/10.1016/j.nanoen.2023.108202).

References

- L. Pan, S. Sun, Y. Chen, P. Wang, J. Wang, X. Zhang, J.J. Zou, Z.L. Wang, Advances in piezo-phototronic effect enhanced photocatalysis and photoelectrocatalysis, *Adv. Energy Mater.* 10 (2020) 2000214.
- Q. Liu, D. Zhai, Z. Xiao, C. Tang, Q. Sun, C.R. Bowen, H. Luo, D. Zhang, Piezo-photoelectronic coupling effect of BaTiO₃@TiO₂ nanowires for highly concentrated dye degradation, *Nano Energy* 92 (2022), 106702.
- F. Mushtaq, X.Z. Chen, H. Torlakcik, C. Steuer, M. Hoop, E.C. Siringil, X. Marti, G. Limburg, P. Stipp, B.J. Nelson, Magneto-electrically driven catalytic degradation of organics, *Adv. Mater.* 31 (2019), 1901378.
- F. Mushtaq, X.Z. Chen, A. Veciana, M. Hoop, B.J. Nelson, S. Pané, Magneto-electric reduction of chromium (VI) to chromium (III), *Appl. Mater. Today* 26 (2022), 101339.
- F. Mushtaq, X.Z. Chen, H. Torlakcik, B.J. Nelson, S. Pané, Enhanced catalytic degradation of organic pollutants by multi-stimuli activated multiferroic nanoarchitectures, *Nano Res.* 13 (2020) 2183–2191.
- D. Kim, I. Efe, H. Torlakcik, A. Terzopoulou, A. Veciana, E. Siringil, F. Mushtaq, C. Franco, D. von Arx, S. Sevim, Magneto-electric effect in hydrogen harvesting: magnetic field as a trigger of catalytic reactions, *Adv. Mater.* 34 (2022), 2110612.
- T. Wang, L. Chen, C. Chen, M. Huang, Y. Huang, S. Liu, B. Li, Engineering catalytic interfaces in Cu²⁺/CeO₂-TiO₂ photocatalysts for synergistically boosting CO₂ reduction to ethylene, *ACS Nano* 16 (2022) 2306–2318.
- P. Wang, S. Fan, X. Li, J. Wang, Z. Liu, Z. Niu, M.O. Tadó, S. Liu, Single Pd atoms synergistically manipulating charge polarization and active sites for simultaneously photocatalytic hydrogen production and oxidation of benzylamine, *Nano Energy* 95 (2022), 107045.
- F. Mushtaq, X.Z. Chen, S. Stauffert, H. Torlakcik, X. Wang, M. Hoop, A. Gerber, X. Li, J. Cai, B.J. Nelson, On-the-fly catalytic degradation of organic pollutants using magneto-photosensitive bacteria-templated microcleaners, *J. Mater. Chem. A* 7 (2019) 24847–24856.
- Y. Zhao, G. Chen, T. Bian, C. Zhou, G.I. Waterhouse, L.Z. Wu, C.H. Tung, L.J. Smith, D. O'Hare, T. Zhang, Defect-rich ultrathin ZnAl-layered double hydroxide nanosheets for efficient photoreduction of CO₂ to CO with water, *Adv. Mater.* 27 (2015) 7824–7831.
- Y. Zhao, L. Zheng, R. Shi, S. Zhang, X. Bian, F. Wu, X. Cao, G.I. Waterhouse, T. Zhang, Alkali etching of layered double hydroxide nanosheets for enhanced photocatalytic N₂ reduction to NH₃, *Adv. Energy Mater.* 10 (2020) 2002199.
- L. Liu, H. Huang, F. Chen, H. Yu, N. Tian, Y. Zhang, T. Zhang, Cooperation of oxygen vacancies and 2D ultrathin structure promoting CO₂ photoreduction performance of Bi₄Ti₃O₁₂, *Sci. Bull.* 65 (2020) 934–943.
- Y. Zhang, D. Yao, B. Xia, H. Xu, Y. Tang, K. Davey, J. Ran, S.-Z. Qiao, ReS₂ nanosheets with in situ formed sulfur vacancies for efficient and highly selective photocatalytic CO₂ reduction, *Small Sci.* 1 (2021), 2000052.
- H. Bai, S.H. Lam, J. Yang, X. Cheng, S. Li, R. Jiang, L. Shao, J. Wang, A schottky-barrier-free plasmonic semiconductor photocatalyst for nitrogen fixation in a “one-stone-two-birds” manner, *Adv. Mater.* 34 (2022) 2104226.
- H. Fatima, M.R. Azhar, Y. Zhong, Y. Arafat, M. Khiadani, S. Shao, Rational design of ZnO-zeolite imidazole hybrid nanoparticles with reduced charge recombination for enhanced photocatalysis, *J. Colloid Interface Sci.* 614 (2022) 538–546.
- Q. Liu, W. Zhao, Z. Ao, T. An, Photo-piezoelectric synergistic degradation of typical volatile organic compounds on BaTiO₃, *Chin. Chem. Lett.* 33 (2022) 410–414.
- R. Pagano, C. Ingrassio, G. Giancane, L. Valli, S. Bettini, Wet synthesis of elongated hexagonal ZnO microstructures for applications as photo-piezoelectric catalysts, *Materials* 13 (2020) 2938.
- F. Mushtaq, X.Z. Chen, M. Hoop, H. Torlakcik, E. Pellicer, J. Sort, C. Gattinoni, B. J. Nelson, S. Pané, Piezoelectrically enhanced photocatalysis with BiFeO₃ nanostructures for efficient water remediation, *Iscience* 4 (2018) 236–246.
- Q. Sun, D. Zhang, G. Xue, Q. Liu, X. Zhou, Z. Pei, H. Luo, L. Zhu, Piezo-assisted photoelectric catalysis degradation for dyes and antibiotics by Ag dots-modified NaNbO₃ powders, *Ceram. Int.* (2022).
- M. Ismail, Z. Wu, L. Zhang, J. Ma, Y. Jia, Y. Hu, Y. Wang, High-efficient synergy of piezocatalysis and photocatalysis in bismuth oxychloride nanomaterial for dye decomposition, *Chemosphere* 228 (2019) 212–218.
- D. Xiang, Z. Liu, M. Wu, H. Liu, X. Zhang, Z. Wang, Z.L. Wang, L. Li, Enhanced piezo-photoelectric catalysis with oriented carrier migration in asymmetric Au-ZnO nanorod array, *Small* 16 (2020) 1907603.
- X. Zhou, Q. Sun, D. Zhai, G. Xue, H. Luo, D. Zhang, Excellent catalytic performance of molten-salt-synthesized Bi_{0.5}Na_{0.5}TiO₃ nanorods by the piezo-phototronic coupling effect, *Nano Energy* 84 (2021), 105936.
- M. Ji, J.H. Kim, C.-H. Ryu, Y.-I. Lee, Synthesis of self-modified black BaTiO_{3-x} nanoparticles and effect of oxygen vacancy for the expansion of piezocatalytic application, *Nano Energy* 95 (2022), 106993.
- M. Shen, Y. Shi, Z. Wang, T. Wu, L. Hu, L. Wu, Enhanced photocatalytic benzyl alcohol oxidation over Bi₄Ti₃O₁₂ ultrathin nanosheets, *J. Colloid Interface Sci.* 608 (2022) 2529–2538.
- Y. Zhang, J. Gao, Z. Chen, Z. Lu, Enhanced photocatalytic performance of Bi₄Ti₃O₁₂ nanosheets synthesized by a self-catalyzed fast reaction process, *Ceram. Int.* 44 (2018) 23014–23023.
- T. Cheng, W. Gao, H. Gao, S. Wang, Z. Yi, X. Wang, H. Yang, Piezocatalytic degradation of methylene blue, tetrabromobisphenol A and tetracycline hydrochloride using Bi₄Ti₃O₁₂ with different morphologies, *Mater. Res. Bull.* 141 (2021), 111350.
- Z. Hu, K. Li, X. Wu, N. Wang, X. Li, Q. Li, L. Li, K. Lv, Dramatic promotion of visible-light photoreactivity of TiO₂ hollow microspheres towards NO oxidation by introduction of oxygen vacancy, *Appl. Catal. B: Environ.* 256 (2019), 117860.
- S. Tu, H. Huang, T. Zhang, Y. Zhang, Controllable synthesis of multi-responsive ferroelectric layered perovskite-like Bi₄Ti₃O₁₂: Photocatalysis and piezoelectric-catalysis and mechanism insight, *Appl. Catal. B: Environ.* 219 (2017) 550–562.
- E. Lin, Z. Kang, J. Wu, R. Huang, N. Qin, D. Bao, BaTiO₃ nanocubes/cuboids with selectively deposited Ag nanoparticles: efficient piezocatalytic degradation and mechanism, *Appl. Catal. B: Environ.* 285 (2021), 119823.
- Q. Tang, J. Wu, D. Kim, C. Franco, A. Terzopoulou, A. Veciana, J. Puigmartí-Luis, X.Z. Chen, B.J. Nelson, S. Pané, Enhanced piezocatalytic performance of BaTiO₃ nanosheets with highly exposed {001} facets, *Adv. Funct. Mater.* (2022), 2202180.
- M. Dong, X. Wang, X.Z. Chen, F. Mushtaq, S. Deng, C. Zhu, H. Torlakcik, A. Terzopoulou, X.H. Qin, X. Xiao, 3D-printed soft magneto-electric microswimmers for delivery and differentiation of neuron-like cells, *Adv. Funct. Mater.* 30 (2020), 1910323.

- [32] J. Wu, N. Qin, E. Lin, B. Yuan, Z. Kang, D. Bao, Synthesis of $\text{Bi}_4\text{Ti}_3\text{O}_{12}$ decussated nanoplates with enhanced piezocatalytic activity, *Nanoscale* 11 (2019) 21128–21136.
- [33] P. Wang, X. Li, S. Fan, Z. Yin, L. Wang, M.O. Tadó, S. Liu, Piezotronic effect and oxygen vacancies boosted photocatalysis C-N coupling of benzylamine, *Nano Energy* 83 (2021), 105831.
- [34] C. Wang, F. Chen, C. Hu, T. Ma, Y. Zhang, H. Huang, Efficient piezocatalytic H_2O_2 production of atomic-level thickness $\text{Bi}_4\text{Ti}_3\text{O}_{12}$ nanosheets with surface oxygen vacancy, *Chem. Eng. J.* 431 (2022), 133930.
- [35] Z. Kang, E. Lin, N. Qin, J. Wu, B. Yuan, D. Bao, Effect of oxygen vacancies and crystal symmetry on piezocatalytic properties of Bi_2WO_6 ferroelectric nanosheets for wastewater decontamination, *Environ. Sci. Nano* 8 (2021) 1376–1388.
- [36] J. Dai, N. Shao, S. Zhang, Z. Zhao, Y. Long, S. Zhao, S. Li, C. Zhao, Z. Zhang, W. Liu, Enhanced piezocatalytic activity of $\text{Sr}_{0.5}\text{Ba}_{0.5}\text{Nb}_2\text{O}_6$ nanostructures by engineering surface oxygen vacancies and self-generated heterojunctions, *ACS Appl. Mater. Interf.* 13 (2021) 7259–7267.
- [37] F. Chen, Z. Ma, L. Ye, T. Ma, T. Zhang, Y. Zhang, H. Huang, Macroscopic spontaneous polarization and surface oxygen vacancies collaboratively boosting CO_2 photoreduction on BiOIO_3 single crystals, *Adv. Mater.* 32 (2020) 1908350.
- [38] P. Wang, X. Li, S. Fan, X. Chen, M. Qin, D. Long, M.O. Tadó, S. Liu, Impact of oxygen vacancy occupancy on piezo-catalytic activity of BaTiO_3 nanobelt, *Appl. Catal. B: Environ.* 279 (2020), 119340.
- [39] Z. Xie, X. Tang, J. Shi, Y. Wang, G. Yuan, J.-M. Liu, Excellent piezo-photocatalytic performance of $\text{Bi}_4\text{Ti}_3\text{O}_{12}$ nanoplates synthesized by molten-salt method, *Nano Energy* 98 (2022), 107247.
- [40] X. Zhou, B. Shen, J. Zhai, N. Hedin, Reactive oxygenated species generated on iodide-doped $\text{BiVO}_4/\text{BaTiO}_3$ heterostructures with Ag/Cu nanoparticles by coupled piezophototronic effect and plasmonic excitation, *Adv. Funct. Mater.* 31 (2021), 2009594.
- [41] C. Hu, H. Huang, F. Chen, Y. Zhang, H. Yu, T. Ma, Coupling piezocatalysis and photocatalysis in $\text{Bi}_4\text{NbO}_8\text{X}$ (X= Cl, Br) polar single crystals, *Adv. Funct. Mater.* 30 (2020), 1908168.
- [42] X. Zhao, H. Yang, Z. Cui, R. Li, W. Feng, Enhanced photocatalytic performance of Ag- $\text{Bi}_4\text{Ti}_3\text{O}_{12}$ nanocomposites prepared by a photocatalytic reduction method, *Mater. Technol.* 32 (2017) 870–880.
- [43] C. Du, D. Li, Q. He, J. Liu, W. Li, G. He, Y. Wang, Design and simple synthesis of composite $\text{Bi}_{12}\text{TiO}_{20}/\text{Bi}_4\text{Ti}_3\text{O}_{12}$ with a good photocatalytic quantum efficiency and high production of photo-generated hydroxyl radicals, *Phys. Chem. Chem. Phys.* 18 (2016) 26530–26538.
- [44] B. Bai, H. Arandiyani, J. Li, Comparison of the performance for oxidation of formaldehyde on nano- Co_3O_4 , 2D- Co_3O_4 , and 3D- Co_3O_4 catalysts, *Appl. Catal. B: Environ.* 142 (2013) 677–683.
- [45] D.-M. Liu, J.-T. Zhang, C.-C. Jin, B.-B. Chen, J. Hu, R. Zhu, F. Wang, Insight into oxygen-vacancy regulation on piezocatalytic activity of $(\text{Bi}_{1/2}\text{Na}_{1/2})\text{TiO}_3$ crystallites: Experiments and first-principles calculations, *Nano Energy* 95 (2022), 106975.
- [46] J. Yan, L. Hu, L. Cui, Q. Shen, X. Liu, H. Jia, J. Xue, Synthesis of disorder-order TaON homojunction for photocatalytic hydrogen generation under visible light, *J. Mater. Sci.* 56 (2021) 9791–9806.
- [47] G. Li, R. Huang, C. Zhu, G. Jia, S. Zhang, Q. Zhong, Effect of oxygen vacancies and its quantity on photocatalytic oxidation performance of titanium dioxide for NO removal, *Colloids Surf. A: Physicochem. Eng. Asp.* 614 (2021), 126156.